Elucidation of Peptide-Directed Palladium Surface Structure for Biologically Tunable Nanocatalysts

Nicholas M. Bedford,[*,†,‡,▽,⊗] Hadi Ramezani-Dakhel,[§,▽] Joseph M. Slocik,[†] Beverly D. Briggs,[‡] Yang Ren,[⊥] Anatoly I. Frenkel,[∥] Valeri Petkov,[#] Hendrik Heinz,[*,§] Rajesh R. Naik,[*,†] and Marc R. Knecht[*,‡]

[†]Materials and Manufacturing Directorate, Air Force Research Laboratory, Wright-Patterson AFB, Ohio 45433, United States, [‡]Department of Chemistry, University of Miami, Coral Gables, Florida 33146, United States, [§]Department of Polymer Engineering, University of Akron, Akron, Ohio 44325, United States, [⊥]X-ray Science Division, Argonne National Laboratory, Argonne, Illinois 60439, United States, [∥]Department of Physics, Yeshiva University, New York, New York 10016, United States, and [#]Department of Physics, Central Michigan University, Mt. Pleasant, Michigan 48858, United States. [▽]N.M.B. and H.R.-D. contributed equally. [⊗]Present address: Applied Chemicals and Materials Division, National Institute of Standards and Technology, Boulder, Colorado 80305, United States.

ABSTRACT Peptide-enabled synthesis of inorganic nanostructures represents an avenue to access catalytic materials with tunable and optimized properties. This is achieved *via* peptide complexity and programmability that is missing in traditional ligands for catalytic nanomaterials. Unfortunately, there is limited information available to correlate peptide sequence to particle structure and catalytic activity to date. As such, the application of peptide-enabled nanocatalysts remains limited to trial and error approaches. In this paper, a hybrid experimental and computational approach is introduced to systematically elucidate biomolecule-dependent structure/function relationships for peptide-capped Pd nanocatalysts. Synchrotron X-ray techniques were used to uncover substantial particle surface structural disorder, which was dependent upon the amino acid sequence of the peptide capping ligand. Nanocatalyst configurations were then determined directly from experimental data using reverse Monte Carlo methods and further refined using molecular dynamics simulation, obtaining thermodynamically stable peptide-Pd nanoparticle configurations. Sequence-dependent catalytic property differences for C—C coupling and olefin hydrogenation were then elucidated by identification of the catalytic active sites at the atomic level and quantitative prediction of relative reaction rates. This hybrid methodology provides a clear route to determine peptide-dependent structure/function relationships, enabling the generation of guidelines for catalyst design through rational tailoring of peptide sequences.
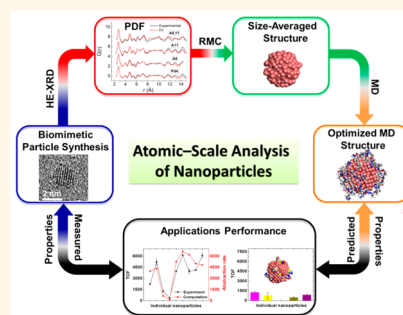
KEYWORDS: biotemplating · peptides · atomic pair distribution function · molecular dynamics simulations · catalysis

Bioinspired inorganic nanomaterials have received much attention due to the potential to generate novel therapeutics, drug delivery systems, electronics, sensors, and catalysts.[1−10] For example, biofunctionalized metal probes for transfection and for the detection of oligonucleotides have been developed,[11,12] and nanomaterials syntheses with peptides have been explored for the controlled fabrication of biosilica, titania, and noble metal nanostructures.[13−19] A common advantage over traditional synthetic approaches is the use of renewably sourced, complex, and programmable capping agents. By exploiting the complexity found in materials binding peptides, an ultimate goal in peptide-derived nanotechnology is to control the materials properties by rational

sequence design. This is particularly true in non-Edisonian development of catalytic materials, wherein peptide-enabled nanocatalysts have previously demonstrated sequence-dependent catalytic properties.[8,9,20] To fully realize this goal, however, a thorough understanding of the biotic/abiotic interface and atomic-level structural motifs is required. Extensive experimental and computational efforts have thus been employed to determine nanoparticle-bound peptide configurations in an effort to elucidate materials properties,[8,9,19,21−31] yet structural comprehension remains elusive, particularly for irregular surfaces, and hence limits rational nanomaterials property engineering.

Our previous work with peptide-capped Pd nanocatalysts demonstrates the capability to modulate catalytic properties by

TABLE 1. Peptide Sequence, Pd Nanocatalyst Size, Catalytic Properties, and Computed Adsorption Energies

peptide	sequence	size (nm)[a,b]	TOF (Stille coupling)[a,c]	TOF (olefin hydrogenation)[c]	adsorption energy (kcal/mol)[d]
Pd4	TSNAVHPTLRHL	2.1 ± 0.4	2200 ± 100	5000 ± 200	−34.7 ± 1.1
A6	TSNAVAPTLRHL	2.2 ± 0.7	5200 ± 400	6100 ± 200	−26.8 ± 1.0
A11	TSNAVHPTLRAL	2.6 ± 0.4	1300 ± 10	2900 ± 700	−14.5 ± 1.0
A6,11	TSNAVAPTLRAL	2.8 ± 0.7	360 ± 20	2600 ± 300	−28.2 ± 1.0
C6	TSNAVCPTLRHL	2.2 ± 0.3	3960 ± 30	1300 ± 200	−23.0 ± 1.0
C11	TSNAVHPTLRCL	2.4 ± 0.4	6140 ± 60	800 ± 500	−24.0 ± 1.0
C6,11	TSNAVCPTLRCL	2.3 ± 0.4	4000 ± 300	0	−22.5 ± 1.0
C6A11	TSNAVCPTLRAL	2.4 ± 0.4	4100 ± 70	500 ± 200	−35.0 ± 1.0
A6C11	TSNAVAPTLRCL	2.4 ± 0.4	6100 ± 300	900 ± 100	−20.6 ± 1.0

[a] Data taken from our previous reports.[8,9] [b] Average diameters from HRTEM. [c] Moles of product (mol Pd × h)$^{-1}$, 0.05 mol% Pd [d] The reported values are the computed adsorption energies per peptide molecule.

altering amino acid content (see Table 1).[8,9,16] Sub-4 nm Pd nanocatalysts were synthesized using the biocombinatorially derived Pd4 peptide (TSNAVHPTLRHL) and various one or two-site amino acid substitution analogues at the strongly interacting histidines.[8,9,16,32] Remarkably, these minor alterations in the native Pd4 sequence result in nanocatalysts with varying turnover frequencies (TOFs) for Stille coupling reactivity.[8,9] Catalytic differences were initially explained in terms of peptide orientation and total coverage at the biotic/abiotic interface, which affects the availability of reactive Pd surface atoms.[8,9] Although such considerations are likely to play a role in the catalytic activity, the underlying presumption is that the available catalytic Pd atoms on the different particles are structurally similar, thus not contributing to the observed catalytic property differences. Yet given the presence of Pd-binding peptides in solution with $PdCl_4^{2-}$ during reduction and growth, it is probable that variation in the peptide composition and secondary structure imparts atomic-scale structural differences at the nanoparticle surface. Such variations likely have a profound effect on the formation of catalytically active Pd, where elucidation of such structural detail would support the development of design rules to optimize nanomaterial reactivity.

In this contribution, a hybrid experimental and computational approach is taken to examine sequence-dependent structure/function relationships at the atomic level by using extensive structural characterization methods as the foundation of the investigation. Atomic pair distribution function (PDF) analysis of high-energy X-ray diffraction (HE-XRD) patterns and X-ray absorption fine-structure spectroscopy (XAFS) are used to probe atomic-scale structure details of peptide-derived Pd nanocatalysts. These techniques, sensitive at the subangstrom level, reveal structural differences over varying length scales for each peptide-capped nanocatalyst (Table 1). Following structural modeling of the experimental data, molecular dynamics (MD) simulations were performed in aqueous solution with binding peptide monolayers to obtain thermodynamically stable atomic arrangements representative of the complete 3D structure of the peptide-capped Pd catalysts. These configurations were used to uncover sequence-dependent structure/function relationships for mechanistically different C–C coupling and olefin hydrogenation reactions resolving catalytically active sites for both systems. Extensive experimental structural studies reveal significant, and unexpected, nanoparticle structural disorder that serves as the foundation to computationally assess and predict catalytic properties that could not otherwise be elucidated using either experimental or computational methods alone. The approaches demonstrated in this contribution are readily applicable to similar heterogeneous catalytic systems and electrocatalysts, opening up a new avenue to understanding structure/property relationships of complex bioinspired nanocatalysts.

RESULTS AND DISCUSSION

Pd nanocatalysts were synthesized with the peptides listed in Table 1 and lyophilized to powders for structure characterization. Swapping of histidine residues at the 6 and 11 position with alanine (weaker binding) and cysteine (stronger binding) was performed to vary site-specific binding strengths of the peptide. X-ray absorption near edge structure (XANES) data for the cysteine analogues (Supporting Information Figure S1) show similarities between nanoparticles yet stark contrast from bulk Pd. This difference in features from the XANES data indicates chemical and structural differences between bulk Pd and the Pd nanocatalyst, likely a contribution of unreduced Pd^{2+} in the sample.[25,33] After background subtraction and edge-step normalization, the extended XAFS (EXAFS) data was converted to k-space, k^2-weighted, and Fourier transformed into r-space as shown in Figure 1a. The EXAFS data for the Pd nanocatalysts made from cysteine analogues of Pd4 show characteristic features for Pd–Pd distances at 2.5 Å and a broader peak in the lower-r range corresponding to nanoparticle-peptide interactions (Figure 1a). Fitting of the r-space data (Supporting Information, Figure S2) yields Pd–Pd, Pd–O/N and Pd–S/Cl coordination numbers (CNs),
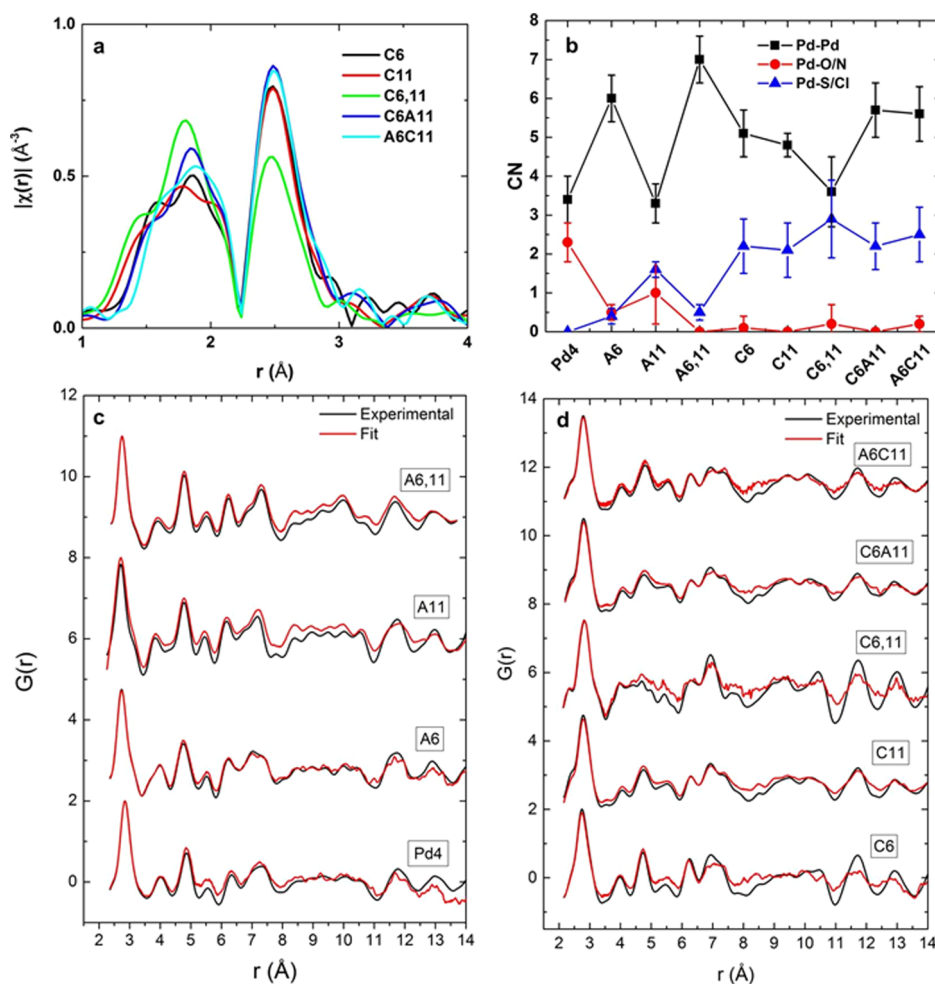
Figure 1. Structural characterization of peptide-capped Pd nanoparticles. (a) *r*-space EXAFS data of Pd capped with cysteine analogues of Pd4, **(b)** coordination numbers (CN) of Pd−Pd, Pd−O/N, Pd−S/Cl as determined by modeling of the EXAFS data, **(c and d)** atomic PDFs of peptide capped Pd nanoparticles (black line) and corresponding RMC modeling (red line). PDFs are vertically offset for clarity.

as shown in Figure 1b, compared to known values for the noncysteine-based materials.[25,33] The CNs reflect all atomic species in the nanoparticle sample. Unfortunately, EXAFS is unable to distinguish between O and N or S and Cl due to similarities in atomic number, and thus the EXAFS results are reported as a combined value for the two elements. Pd−Pd CNs for particles capped with cysteine analogues of Pd4 show sequence-based trends. C6 and C11, consisting of one cysteine residue at the 6 or 11 position, respectively, yielded similar average Pd−Pd CNs of 5.1 ± 0.6 and 4.8 ± 0.3. Replacement of both histidines with either an alanine or cysteine residue (A6C11 and C6A11) resulted in an increase in average Pd−Pd CN to 5.7 ± 0.7 and 5.6 ± 0.7, respectively, suggesting the placement of an alanine at either position enhances the degree of local atomic ordering due to the presence of a weakly interacting functionality at the key locations in the sequence. Placing cysteine residues at both the 6 and 11 positions (C6,11) resulted in a decrease in average Pd−Pd CN to 3.7 ± 0.9. Information regarding Pd−peptide interactions are obtainable from *r*-space

fitting (Figure 1b, blue and red symbols/lines). Unsurprisingly, CNs for Pd−S/Cl are much higher than those for Pd−O/N in the cysteine analogues, demonstrating the high affinity of the cysteine residues to Pd. While Pd−thiol interactions are likely the major contributor to Pd−S/Cl CNs, Pd−Cl interactions have been noted for nonthiol containing peptide generated materials (Figure 1b) and cannot be ruled out.[33] Minimal Pd−O/N contributions were obtained for Pd capped with cysteine analogues of Pd4, further indicating binding exclusively through the thiol functionalities. Note that Pd−O/N CNs are readily obtainable from Pd capped with Pd4 and corresponding alanine analogues. Thereby, as previously observed,[33] coordination numbers lower than expectations can result from interactions between unreduced Pd^{2+} ions and peptides prior to reduction with 10-fold excess of $NaBH_4$. For example, specific Pd^{2+}-peptide interactions in case of weakly binding A11 may explain an overall lower Pd−Pd CN in comparison to more strongly binding C11. A summary of all relevant EXAFS data is given in Table S1.

While XAFS is a valuable method for probing local structural and chemical environments, information sensitive to the atomic arrangement beyond the first coordination sphere is needed to build accurate structural models. Such information can be obtained using atomic PDF analysis of HE-XRD patterns. Atomic PDFs of Pd nanocatalysts were obtained by converting HE-XRD patterns first into total reduced structure factors, $Q[S(Q) - 1]$, (Supporting Information, Figure S3) and Fourier transformed into atomic PDFs, $G(r) = 4\pi r[\rho(r) - \rho_0]$, wherein r is the atomic pair distance and $\rho(r)$ and ρ_0 are the local and average atomic densities, respectively (see Supporting Information). As evident from Figure S3, peaks that may be described in terms of a face-centered cubic (fcc) lattice are observed. Minor sharp peaks of substantially lower intensity are also observable, which are attributed to Pd^{2+} in the lyophilized powder.[25,33] Because of the sharp, Bragg-like character of these peaks and their comparatively smaller integral intensity, these features contribute very little to the important features in the PDFs due to the nature of the Fourier transform used to obtain the PDF. PDFs of the Pd nanocatalysts, shown in Figure 1c and 1d (black lines) reveal clear sequence-dependent structural differences. Overall, the particles resemble a disordered fcc arrangement, with structural differences noted at various pair lengths for all Pd nanocatalysts. Of particular note, the cysteine-based analogues tend to exhibit the largest deviation from an ideal fcc lattice as compared to the Pd4 and alanine analogues. Significant broadening and shifting of Pd atomic pairs peaks were evident for all nanocatalysts possessing surface thiol functionality, while also displaying a low-r shoulder at ~2.3 Å for strong Pd–S atomic pairs. A decrease in structural order was anticipated since thiols are known to invoke structural disorder in other metallic nanomaterials,[34−37] either through surface relaxation and/or the formation of staple motifs.[38,39] A closer examination of the PDFs yielded additional structural information. For example, the full width at half-maximum (fwhm) of the first PDF peak (Supporting Information Table S3, Figure S4) can also be used to measure the relative degree of structural order between nanocatalysts, as this quantity reflects the structural distortions in the first atomic coordination sphere. The Pd4 and corresponding alanine analogues have fwhms ranging from 0.36 to 0.43 Å, while the cysteine analogues of Pd4 have fwhms ranging from 0.45 to 0.54 Å. This increase in fwhm for the cysteine analogues is indicative of a less defined first coordination sphere, which is consistent with the known disorder inducing behavior of thiol groups as stated above. Note that these trends are similar to those seen in EXAFS, but that the CNs from EXAFS consist of both reduced and unreduced Pd, whereas unreduced Pd contributions are effectively masked in the PDF. Further examination of atomic PDFs at longer atomic pair distances shows additional structural differences between each sample (Supporting Information, Figure S4). In the 3.5−11.0 Å range, atomic pairs are more distinct for Pd4 and the alanine analogues when compared to the cysteine analogues. Again, this is evidence of a more ordered nanoparticle for the noncysteine samples. Note that for the A6,11-capped nanoparticle sample with more pronounced features in the PDF, the particle is ~1 nm larger than the remaining samples, and hence has a lower fraction of surface atoms. For comparison, the atomic PDF of Pd black (bulk precipitation of $PdCl_4^{2-}$ with $NaBH_4$) was collected (Supporting Information, Figure S5). The peaks of Pd black are much better defined than those for Pd nanocatalysts, reflecting the presence of long-range periodic atomic order. Overall, the atomic PDF and XAFS analyses demonstrate clear atomic-scale structural differences associated with changes at key locations in the peptide sequence, which ultimately affect their catalytic properties.

The experimental PDFs of the nanocatalysts were then modeled using reverse Monte Carlo (RMC) simulations (red line, Figure 1c and d). RMC simulations are an established and ideal technique for modeling structure functions of highly disordered materials that requires no crystallographic information.[36,40] Using the CN values obtained from XAS modeling as a guide, resulting RMC nanocatalyst configurations model the PDF data of the peptide-derived materials reasonably well, as shown in Figure 2 (RMC column). The resulting configurations, modeled directly from experimental data, exhibited a significant amount of high-energy surface Pd atoms, and are vastly more disordered than commonly presumed idealized single crystals. Bond angle distributions were calculated from the RMC-generated configurations as well, further showing a disordered fcc-type structure (Supporting Information, Figure S6). Additional analysis of the configurations demonstrated that the majority of disordered Pd is present at the surface, with the interior atoms better resembling an fcc arrangement typically observed in high-resolution transmission electron microscopy (HRTEM) (Figure 2). No such constraints were given in the RMC simulation. As such, these disordered nanocatalyst surfaces are likely a direct result of the capping peptide, which showed sequence-dependent differences in surface disorder.

While RMC is a valuable technique to model experimental structure functions, the configurations are entropically driven and can result in an overestimation of atomic disorder. Furthermore, the RMC generated configurations represent an average structure of a large number of nanoparticles used to generate the diffraction pattern, which will unavoidably have a distribution of sizes and atomic structures. Therefore, the manifestation of all size/structural differences into one singular configuration likely exaggerates structural
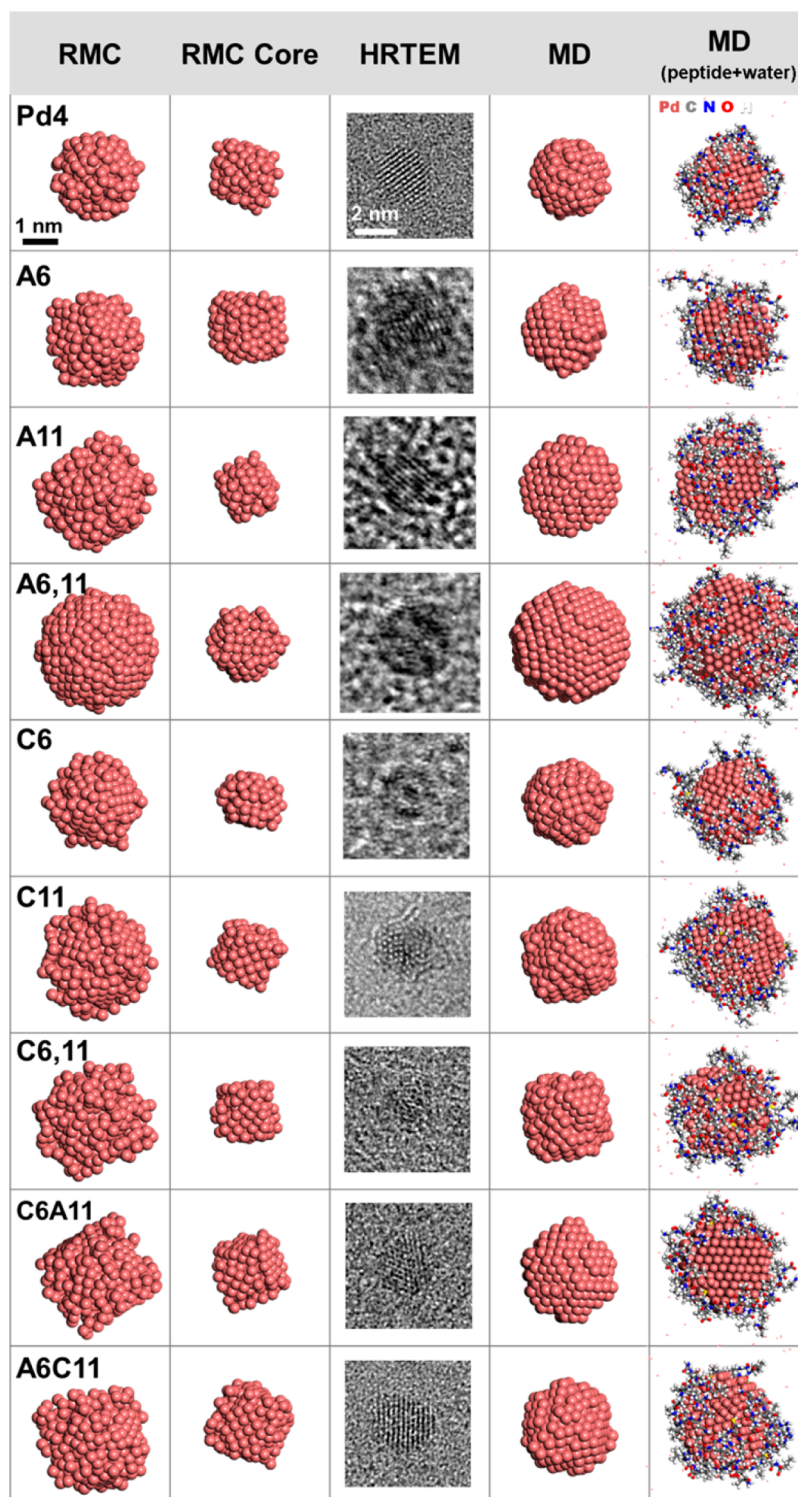
Figure 2. Morphology of the nanocatalysts and of surface-adsorbed peptides from experimental structure studies, HRTEM, and simulations. RMC denotes the structures generated by reverse Monte Carlo simulations of atomic PDFs. These structures exemplify a size-averaged morphology of the synthesized Pd particles represented using a singular configuration. RMC Core denotes the interior of the RMC structures, which better resemble the nanocatalysts observed with HRTEM. MD denotes thermodynamically stable morphologies of the particles as well as of particles in contact with a superficial monolayer of corresponding peptides using molecular dynamics simulation. RMC simulations matching PDF data provided the initial 3D arrangements of the particles for MD simulations.

disorder. On the other hand, MD simulations alone could not reproduce meaningful PDF data without experimental information on the number of atoms

and particle shape. Here, we employ a hybrid approach wherein RMC produced models of single averaged particles to be further used in MD simulations to relax

atomic positions and achieve stable morphologies. These simulations were completed using the established CHARMM-INTERFACE force field,[38,39] resulting in energetically more stable structures than the RMC-generated configurations (Figure 2 and Movie S1). Note that MD optimized configurations also do not exhibit perfect nanoscale crystallinity and contain significant surface metal structural disorder. From these particle configurations, MD simulations were performed to incorporate a monolayer of capping peptide in aqueous solution on the nanocatalyst surface to determine the spatial location and binding energies of peptides (see Methods and Movie S1 for details of calculations). The computationally derived binding energies per peptide are provided in Table 1, while MD generated configurations are shown in Figure 2. Computed adsorption energies lower than −15 kcal/mol per peptide (Table 1) indicate a strong interaction between the peptides and particles, which is likely the origin of perturbed bulk crystal growth.[41,42] The MD calculations indicated that the parent Pd4 peptide and C6A11 analogue adsorb more strongly to the particles compared to the other seven analogues (Table 1). Furthermore, the presence of cysteine in some of the peptide sequences pins the biomolecules to the surface and reduces the conformational flexibility of the bound ligands, while peptides without cysteine possess more transitional and conformational flexibility at the biotic/abiotic interface.[8]

The resulting experimentally derived and MD optimized configurations were then used to uncover sequence-dependent catalytic properties for Stille coupling reactions. Previously, we have shown that these materials are reactive for the coupling of 4-iodobenzoic acid (4-IBA) with trichlorophenyl stannane (PhSnCl$_3$) to generate biphenylcarboxylic acid (BPCA) at low catalyst loading in environmentally friendly aqueous solvents.[8,9,16] Mechanistically it is anticipated that 4-IBA oxidizes and abstracts a surface Pd atom from the nanocatalyst,[28,40] forming a Pd^{2+}-complex in solution. A C—C bond is then formed upon transmetalation with PhSnCl$_3$ and reductive elimination to produce the biphenyl product (Figure 3a). In this sequence of reactions, it was previously suggested that the abstraction of Pd atoms from the surface of the nanoparticle is the rate-determining step.[31] The catalytic efficiency is therefore highly dependent on the amount of energy required to remove individual Pd atoms from the surface that is in turn dictated by surface structural disorder. The computation of the reaction rate first involved the analysis of the abstraction energies of all individual atoms from the particle surface using the CHARMM-INTERFACE force field (Figure 3b, and Supporting Information, Figures S7 and S8).[43,44] Then, the sum of Boltzmann-weighted individual abstraction energies, normalized by the total number of atoms in the nanoparticle, yields the total
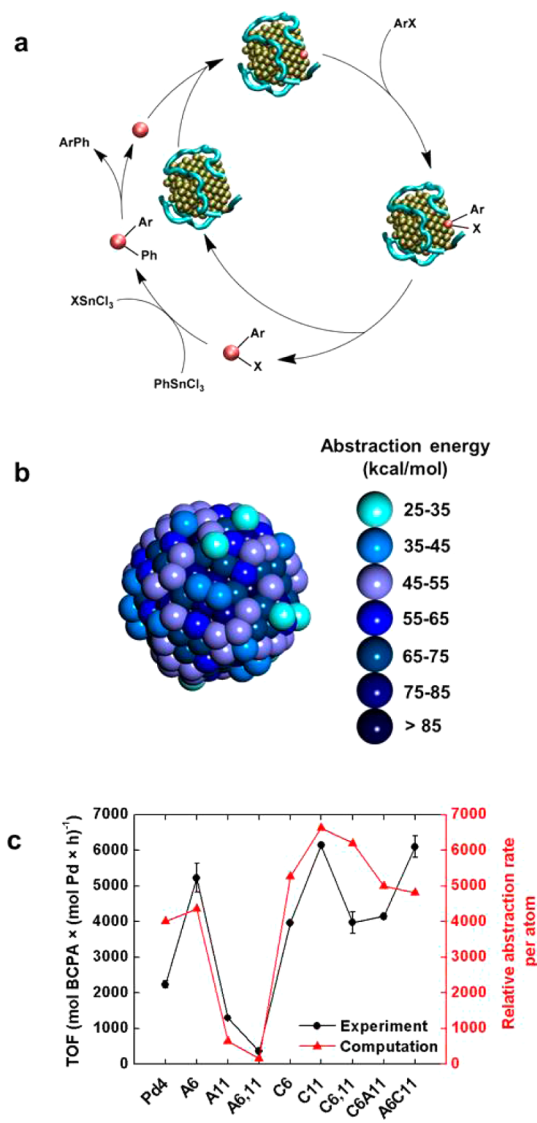

Figure 3. Correlation of catalytic performance in experiment with estimates from MD simulations for Stille C—C coupling. (a) Mechanism of the Stille coupling reaction, **(b)** illustration of the abstraction energies for individual atoms of the Pd4 nanocatalyst, indicating the locations of the lowest energy Pd atoms (*i.e.*, active sites), **(c)** correlation of the computed leaching rate of Pd nanoparticles with the measured catalytic TOF values for the Stille reaction.[8,9]

relative rate of atom abstraction, *i.e.*, the computed relative TOF (Figure 3c, and Supporting Information, section S1.2).[31] As shown in Figure 3c, the computed relative abstraction rate per atom correlates well with the experimental TOFs in the Stille coupling reaction, indicating that the model structures of the surface of the nanocatalysts, which are ultimately dictated by the peptide sequence, are remarkably realistic. In general, the cysteine analogues introduced greater surface distortions at the Pd surface through the strong Pd—S bonds, resulting in a higher number of atoms with minimal abstraction energies required for initiation of the Stille reaction. Among the alanine permutations of the Pd4 analogues, A6 shows a critical combination of

peptide binding strength and binding conformation that leads to formation of a nanocatalyst that exhibits a high number of leachable atoms of low abstraction energy.

The vivid correlation between the computed TOFs from experimentally originating configurations and Stille coupling TOFs shows direct sequence-dependent structural and catalytic properties. Consideration of the catalytic mechanism is also important to fully understand structure/function relationships, as disordered surface morphology may not always lead to enhanced catalytic activity. For this purpose, we consider the catalytic hydrogenation of allyl alcohol. This reaction follows a very different mechanism as compared to the atom-leaching C—C coupling process as catalysis occurs strictly at the Pd surface. In particular, the alkene adsorbs onto the hydrogen-saturated metallic surface of the nanocatalyst. Upon substrate adsorption, surface-activated hydrogen atoms bond with the β carbon atom of the olefin, and a σ-bond between a Pd atom and the α carbon atom is formed. This intermediate state facilitates the reductive elimination to the alkane (Figure 4a).[45−47] TOFs for the hydrogenation of allyl alcohol to n-propanol using the peptide-capped Pd nanocatalysts are shown in Figure 4 b,c and Table 1, with strikingly different reactivity trends as compared to the Stille coupling reactions. For the parent Pd4-capped materials, a TOF value of 5000 ± 200 mol product (mol Pd × h)$^{-1}$ was noted, while the particles capped with the alanine analogues yielded TOFs of 6100 ± 200, 2800 ± 300, and 2600 ± 300 mol product (mol Pd × h)$^{-1}$ for A6, A11, and A6,11-ligands, respectively. For the particles prepared using the cysteine analogues, significantly diminished reactivity is observed. For the C6-capped nanocatalysts, a TOF of 1300 ± 200 mol product (mol Pd × h)$^{-1}$ was obtained that decreased to a value of 800 ± 200 mol product (mol Pd × h)$^{-1}$ for the C11-based structures. The nanoparticles stabilized with the C6A11 and A6C11 peptides demonstrated TOF values of 500 ± 200 and 900 ± 100 mol product (mol Pd × h)$^{-1}$, respectively. Notably, no catalytic activity was observed with the C6,11-capped nanoparticles.

The trends in catalytic activity observed for allyl alcohol hydrogenation were also assessed computationally. Relative TOF values of the Pd nanoparticles capped with the Pd4 and alanine analogue peptides were estimated by calculating the number of allyl alcohol molecules that can be adsorbed on the peptide-covered Pd surface normalized by number of metal atoms in the nanocatalyst (see Supporting Information, section S1.2, for additional details). The computationally estimated TOF values for these systems closely correlate with the measured TOFs (Figure 4b). The relationship suggests that the reaction rate is controlled by the available surface area on the peptide-covered, hydrogen-saturated nanoparticle to allow the approach of allyl alcohol. A slightly
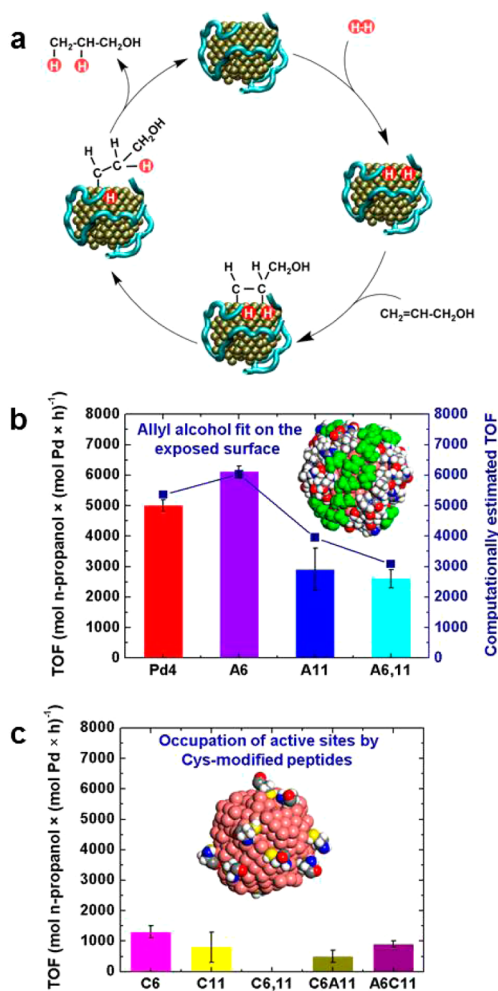

Figure 4. Correlation of catalytic performance in experiment with estimates from MD simulations for olefin hydrogenation. (a) Mechanism of the hydrogenation of allyl alcohol catalyzed by peptide-capped Pd nanoparticles, (b and c) experimental and computational TOFs for the hydrogenation of allyl alcohol (insets show peptide binding to Pd configurations and the available surfaces for hydrogenation (b) or the location of thiol-Pd pinning (c)).

diminished TOF for the Pd4-capped materials can be attributed to the presence of the additional histidine residue, which anchors more of the peptide to the surface, reducing the number of exposed Pd atoms. While A6 and A11 exhibited the same number of histidine residues, the histidine in A11 is neighbored by a conformationally restricted proline, thus forcing more of the peptide directly to the Pd surface and reducing the amount of available metallic surface for substrate adsorption. Conversely, the A6,11-capped particles, which possess no histidine, demonstrated the lowest reactivity for this set of materials. The lower reactivity is likely attributed to the increased particle size (about twice the number of Pd atoms), thus reducing the surface to volume ratio for this system (see Supporting Information), as well as to peptide-Pd interactions through remaining attractive residues such as arginine at position 10 and serine at position 2.

Hydrogenation reactions using the particles stabilized with the cysteine analogue peptides showed very limited reactivity for allyl alcohol hydrogenation. This diminished reactivity is associated with the tightly bound and more restricted peptide orientation at the biotic/abiotic interface due to Pd—S bond formation. The cysteine residues pin the peptide to the metallic surface through semicovalent Pd—S bonds (Figure 4c) and hinder peptide mobility at the biotic—abiotic interface, requiring a significant amount of energy to detach these residues from the surface (see Supporting Information). This pinning effect results in permanent occupation of active sites and dramatically reduces the catalytic activity of the particles, whereas Pd4 and corresponding alanine peptide analogues are more flexible and thus facilitate substrate interactions with the Pd surface. The complete lack of reactivity of the C6,11-capped nanocatalysts further supports the proposed deactivation effect by tight peptide binding.

The sequence-dependent structure/function relationships shown above are only obtainable using this hybrid experimental and computational approach and demonstrate the importance of understanding inorganic atomic-level structure along with the peptide binding effects and morphology at the biotic/abiotic interface to enable predictions. Understanding in atomic-level detail is especially critical for catalytic reactions that proceed by vastly different mechanisms. In Stille coupling, the abstraction energy of surface Pd atoms directly influences the catalytic activity, which is dependent upon the degree of structural disorder at the nanocatalyst surface. As shown above, the surface structure is dictated by the chemical functionality and position of the amino acid residues in the capping peptide, indicating the potential to engineer nanocatalyst surfaces to improve performance characteristics through rational peptide design. For the hydrogenation of allyl alcohol as a strictly surface catalyzed reaction, folding and mobility of the peptide at the nanoparticle surface is more influential in determining catalytic properties. The impact of peptide attachment was reflected by the drastic catalytic differences between the nanocatalysts capped with Pd4 and its alanine analogue peptides as compared to the materials prepared using the cysteine-containing sequences. These observations stress the need in understanding the atomic scale structure of the nanocatalysts as well as the reaction mechanism to elucidate catalytic active sites for particle design with optimal reactivity.

CONCLUSIONS

Overall, this contribution explains how structure/function relationships of peptide-capped Pd nanoparticle catalysts can be elucidated using a hybrid experimental and computational approach to support the rational design of nanocatalysts. Structural characterization techniques show that minor changes in amino acid content strongly influence the structure of the Pd nanocatalysts, resulting in model configurations that exhibit a significant amount of highly disordered surface atoms. Subsequent MD simulations using experimental structure models as a starting point demonstrate the strong dependence of the catalytic activity on the sequence-induced surface disorder and peptide surface morphology at the biotic/abiotic interface. The results also indicate that relying exclusively on experimental or computation methods alone would not be sufficient for a complete analysis of bioinspired nanomaterials, and that the combination of experimental and computational techniques is essential to determine sequence dependent structure/function relationships. The scientific approach demonstrated here can be easily translated to other biomimetic nanostructures, opening a new route to fully understanding sequence-dependent structure/function relationships for the development of nanomaterial surface structural features with tailored functional properties. Follow-on challenges also include *in situ* monitoring of the nanoparticles during and after the reactions to detect potential restructuring processes, as well as to explore the potential participation of surface-bound peptides in the reactions.

METHODS

Synthesis of Peptide-Capped Pd Nanocatalysts. Peptides were synthesized using standard solid-phase FMOC automated peptide synthesis protocols employing a TETRAS model peptide synthesizer (CreoSalus) with reagents purchased from Advanced ChemTech. After preparation, the crude peptides were purified *via* reverse-phase HPLC and confirmed by MALDI-TOF mass spectrometry. All peptide-capped Pd nanoparticle samples were synthesized as described previously.[8,9,16]

XAFS. As-synthesized nanoparticle solutions were lyophilized into powders for XAFS and PDF analysis. XAFS experiments were conducted at the X18B beamline at the National Synchrotron Light Source, Brookhaven National Laboratory. Lyophilized Pd nanoparticle powders were uniformly spread across adhesive tape and examined in transmission mode between 150 eV below and 1350 eV above the Pd K-edge (24,353 eV). The raw data was processed using the Athena program and modeled using the Artemis program from the IFEFFIT XAFS analysis software package using reasonable theoretical contributions.[48] For the *r*-space fits, an amplitude factor of $S_0^2 = 0.885$ was obtained from the transmission XAFS data of a Pd foil. The construction of theoretical contributions for Pd—Pd, Pd—O/N and Pd—S/Cl were obtained from the known crystal structure of bulk Pd, PdO, and PdS, respectively.[49−51] These contributions were combined in Artemis into a total theoretical signal and used for the modeling of all peptide-capped Pd nanoparticles.

PDF Experimentation and Analysis. HE-XRD experiments were performed at the 11-ID-C beamline at the Advanced Photon Source, Argonne National Laboratory. Using 115 keV irradiation and a large area 2-D detector, data was collected over a large region of reciprocal space vectors (0−30 Å^{-1}) in transmission geometry with lyophilized peptide-derived Pd nanocatalysts

placed in 2 mm outer diameter thin-walled quartz capillaries. The raw HE-XRD data was background corrected and converted into their corresponding total structure functions $S(Q)$ using the program RAD[52] *via*

$$S(Q) = 1 + \frac{I^{coh}(Q) - \Sigma c_i |f_i(Q)|^2}{|\Sigma c_i f_i(Q)|^2} \tag{1}$$

wherein $I^{coh}(Q)$ is the coherent part of the HE-XRD pattern and c_i and $f_i(Q)$ are the atomic concentration and X-ray scattering factors respectively for the atomic species i. The atomic pair distribution functions, $G(r)$, were obtained from the Fourier transform of $Q[S(Q) - 1]$ *via*

$$G(r) = \left(\frac{2}{\pi}\right) \int_{Q=0}^{Q_{max}} Q[S(Q) - 1] \sin(Qr) \, dQ \tag{2}$$

Atomic structure studies using PDF analysis are advantageous for materials lacking long-range periodic order, such as nanoscale materials, as $G(r)$ reflect contributions from both diffuse and Bragg features in the diffraction pattern as indicated from the Fourier transform of $S(Q)$ and, furthermore, does not imply any periodicity.[53−56] The atomic PDF is given as $G(r) = 4\pi r(\rho(r) - \rho_0)$, where r is the distance between two atom pairs, $\rho(r)$ is local atomic density, and ρ_0 is the average atomic density. Peaks in the PDF represent distances within the material of a high number of atomic pairs and valleys represent distances of little atomic density. The PDF for nanomaterials may not extend to distances longer than the size of the nanomaterial.

RMC Modeling. Reverse Monte Carlo (RMC) simulations were used to generate structure models directly from the experimental data using the RMC++ program.[57] Spherical structures produced by extending the known unit cell for Pd were used as starting configurations. Initial configurations were generated from the known crystal structure of Pd and extended in a radial fashion to a nanocatalyst diameter equivalent to those found from previous TEM experiments. CNs obtained from XAFS modeling were also used to guide the RMC modeling. The simulations are carried out only by the experimental data and some user inputted restrictions. In RMC, an atom is moved at random from an initial configuration of atoms and a new structure function (here, the atomic PDF) is calculated. If the new PDF provides a better fit to the experimental data, the move is accepted and the algorithm proceeds. Otherwise, the move is disregarded at a certain percentage of moves to prevent the simulation from getting stuck in a local minimum in configuration space. This process is repeated until the computed PDF converges to the experimental PDF in very good detail, with typical agreement factors (R_w) below ∼10%.

Hydrogenation Reactions. Hydrogenation reactions were performed as previously described.[58] Briefly, 0.05 mol% Pd was bubbled with H_2 at room temperature and pressure for 30 min prior to the addition of allyl alcohol. Aliquots were taken at predetermined time intervals for TOF determination. Product analysis was performed *via* gas chromatography (GC: Agilent 7820A) equipped with a DB-ALC1 column and a flame ionization detector (FID) without further purification.

Molecular Dynamics Simulations. All-atom molecular dynamics (MD) simulations were conducted to determine an average relaxed structure of the nanoparticles derived from PDF/RMC atomic positions, as well as the conformation and binding energy of peptides adsorbed on the surface in aqueous solution. The relaxed particle structures with bound peptides according to MD simulations were subsequently employed to identify quantitative correlations with the experimentally observed turnover frequencies (TOFs) of the Pd particles in Stille coupling and hydrogenation reactions. The simulations were carried out with the CHARMM-INTERFACE force field including reactive extensions for thiols and atom abstraction.[43,44]

The relative TOF of the particles in Stille coupling reactions was computed using a previously described reactive MD protocol.[31] First, the abstraction energy E_i of individual Pd atoms was computed as the energy required for the removal of an atom to a distance of at least 1.2 nm away from the surface of the particle using single point energy calculations. Then,

the relative TOF $(TOF)_{C,Stille}$ was calculated as a sum of the Boltzmann-weighted abstraction energies $e^{-E_i/RT}$ of all individual surface atoms (N_S), equal to a cumulative abstraction rate:

$$(TOF)_{C,Stille} \sim \frac{1}{N} \sum_{i=1}^{N_S} e^{-E_i/RT} \tag{3}$$

The result was normalized to the total number of atoms of each particle N to allow direct comparisons with TOF measurements in experiment.

The computation of relative TOFs in the hydrogenation reaction of allyl alcohol was carried out for the particles derived from Pd4 and its alanine mutations. The protocol involved docking of allyl alcohol molecules onto the peptide-covered nanoparticles in equilibrium. The reaction rate was found to be proportional to the number of molecules of allyl alcohol $N_{allylalcohol}$ that can be adsorbed to the available surface area for a given particle shape and specific peptide coverage, normalized by the total number of Pd atoms N that constitute the particle:

$$(TOF)_{C,Hydro} \sim \frac{N_{allylalcohol}}{N} \tag{4}$$

Complete details of molecular models, force fields, simulation protocols, and computation of reaction rates are described in the Supporting Information (section S1 and Movie S1).

Conflict of Interest: The authors declare no competing financial interest.

Supporting Information Available: Supporting Movie S1 and materials and methods. The Supporting Information is available free of charge on the ACS Publications website at DOI: 10.1021/acsnano.5b00168.

REFERENCES AND NOTES

1. Dickerson, M. B.; Sandhage, K. H.; Naik, R. R. Protein- and Peptide-Directed Syntheses of Inorganic Materials. *Chem. Rev.* **2008**, *108*, 4935–4978.

2. Sarikaya, M.; Tamerler, C.; Jen, A. K. Y.; Schulten, K.; Baneyx, F. Molecular Biomimetics: Nanotechnology through Biology. *Nat. Mater.* **2003**, *2*, 577–585.

3. Briggs, B. D.; Knecht, M. R. Nanotechnology Meets Biology: Peptide-based Methods for the Fabrication of Functional Materials. *J. Phys. Chem. Lett.* **2012**, *3*, 405–418.

4. Mirkin, C. A.; Letsinger, R. L.; Mucic, R. C.; Storhoff, J. J. A DNA-Based Method for Rationally Assembling Nanoparticles into Macroscopic Materials. *Nature* **1996**, *382*, 607–609.

5. Schreiber, R.; Do, J.; Roller, E. M.; Zhang, T.; Schuller, V. J.; Nickels, P. C.; Feldmann, J.; Liedl, T. Hierarchical Assembly of Metal Nanoparticles, Quantum Dots and Organic Dyes Using DNA Origami Scaffolds. *Nat. Nanotechnol.* **2014**, *9*, 74–78.

6. Kharlampieva, E.; Slocik, J. M.; Singamaneni, S.; Poulsen, N.; Kroger, N.; Naik, R. R.; Tsukruk, V. V. Protein-Enabled Synthesis of Monodisperse Titania Nanoparticles On and Within Polyelectrolyte Matrices. *Adv. Funct. Mater.* **2009**, *19*, 2303–2311.

7. Nam, K. T.; Kim, D. W.; Yoo, P. J.; Chiang, C. Y.; Meethong, N.; Hammond, P. T.; Chiang, Y. M.; Belcher, A. M. Virus-Enabled Synthesis and Assembly of Nanowires for Lithium Ion Battery Electrodes. *Science* **2006**, *312*, 885–888.

8. Coppage, R.; Slocik, J. M.; Ramezani-Dakhel, H.; Bedford, N. M.; Heinz, H.; Naik, R. R.; Knecht, M. R. Exploiting Localized Surface Binding Effects to Enhance the Catalytic Reactivity of Peptide-Capped Nanoparticles. *J. Am. Chem. Soc.* **2013**, *135*, 11048–11054.

9. Coppage, R.; Slocik, J. M.; Sethi, M.; Pacardo, D. B.; Naik, R. R.; Knecht, M. R. Elucidation of Peptide Effects that Control the Activity of Nanoparticles. *Angew. Chem., Int. Ed.* **2010**, *49*, 3767–3770.

10. So, C. R.; Hayamizu, Y.; Yazici, H.; Gresswell, C.; Khatayevich, D.; Tamerler, C.; Sarikaya, M. Controlling Self-Assembly of Engineered Peptides on Graphite by Rational Mutation. *ACS Nano* **2012**, *6*, 1648–1656.

11. Seferos, D. S.; Giljohann, D. A.; Hill, H. D.; Prigodich, A. E.; Mirkin, C. A. Nano-Flares: Probes for Transfection and mRNA Detection in Living Cells. *J. Am. Chem. Soc.* **2007**, *129*, 15477–15479.

12. Reynolds, R. A.; Mirkin, C. A.; Letsinger, R. L. Homogeneous, Nanoparticle-Based Quantitative Colorimetric Detection of Oligonucleotides. *J. Am. Chem. Soc.* **2000**, *122*, 3795–3796.

13. Brown, S. Metal-Recognition by Repeating Polypeptides. *Nat. Biotechnol.* **1997**, *15*, 269–272.

14. Naik, R. R.; Stringer, S. J.; Agarwal, G.; Jones, S. E.; Stone, M. O. Biomimetic Synthesis and Patterning of Silver Nanoparticles. *Nat. Mater.* **2002**, *1*, 169–172.

15. Chiu, C. Y.; Li, Y. J.; Ruan, L. Y.; Ye, X. C.; Murray, C. B.; Huang, Y. Platinum Nanocrystals Selectively Shaped Using Facet-Specific Peptide Sequences. *Nat. Chem.* **2011**, *3*, 393–399.

16. Pacardo, D. B.; Sethi, M.; Jones, S. E.; Naik, R. R.; Knecht, M. R. Biomimetic Synthesis of Pd Nanocatalysts for the Stille Coupling Reaction. *ACS Nano* **2009**, *3*, 1288–1296.

17. Dickerson, M. B.; Jones, S. E.; Cai, Y.; Ahmad, G.; Naik, R. R.; Kröger, N.; Sandhage, K. H. Identification and Design of Peptides for the Rapid, High-Yield Formation of Nanoparticulate TiO$_2$ from Aqueous Solutions at Room Temperature. *Chem. Mater.* **2008**, *20*, 1578–1584.

18. Whaley, S. R.; English, D. S.; Hu, E. L.; Barbara, P. F.; Belcher, A. M. Selection of Peptides with Semiconductor Binding Specificity for Directed Nanocrystal Assembly. *Nature* **2000**, *405*, 665–668.

19. Puddu, V.; Perry, C. C. Peptide Adsorption on Silica Nanoparticles: Evidence of Hydrophobic Interactions. *ACS Nano* **2012**, *6*, 6356–6363.

20. Li, Y.; Tang, Z.; Prasad, P. N.; Knecht, M. R.; Swihart, M. T. Peptide-Mediated Synthesis of Gold Nanoparticles: Effects of Peptide Sequence and Nature of Binding on Physicochemical Properties. *Nanoscale* **2014**, *6*, 3165–3172.

21. Tamerler, C.; Oren, E. E.; Duman, M.; Venkatasubramanian, E.; Sarikaya, M. Adsorption Kinetics of an Engineered Gold Binding Peptide by Surface Plasmon Resonance Spectroscopy and a Quartz Crystal Microbalance. *Langmuir* **2006**, *22*, 7712–7718.

22. Hnilova, M.; Oren, E. E.; Seker, U. O. S.; Wilson, B. R.; Collino, S.; Evans, J. S.; Tamerler, C.; Sarikaya, M. Effect of Molecular Conformations on the Adsorption Behavior of Gold-Binding Peptides. *Langmuir* **2008**, *24*, 12440–12445.

23. Skelton, A. A.; Liang, T. N.; Walsh, T. R. Interplay of Sequence, Conformation, and Binding at the Peptide-Titania Interface as Mediated by Water. *ACS Appl. Mater. Interfaces* **2009**, *1*, 1482–1491.

24. Heinz, H.; Farmer, B. L.; Pandey, R. B.; Slocik, J. M.; Patnaik, S. S.; Pachter, R.; Naik, R. R. Nature of Molecular Interactions of Peptides with Gold, Palladium, and Pd-Au Bimetal Surfaces in Aqueous Solution. *J. Am. Chem. Soc.* **2009**, *131*, 9704–9714.

25. Coppage, R.; Slocik, J. M.; Briggs, B. D.; Frenkel, A. I.; Heinz, H.; Naik, R. R.; Knecht, M. R. Crystallographic Recognition Controls Peptide Binding for Bio-Based Nanomaterials. *J. Am. Chem. Soc.* **2011**, *133*, 12346–12349.

26. Mirau, P. A.; Naik, R. R.; Gehring, P. Structure of Peptides on Metal Oxide Surfaces Probed by NMR. *J. Am. Chem. Soc.* **2011**, *133*, 18243–18248.

27. Patwardhan, S. V.; Emami, F. S.; Berry, R. J.; Jones, S. E.; Naik, R. R.; Deschaume, O.; Heinz, H.; Perry, C. C. Chemistry of Aqueous Silica Nanoparticle Surfaces and the Mechanism of Selective Peptide Adsorption. *J. Am. Chem. Soc.* **2012**, *134*, 6244–6256.

28. Wright, L. B.; Rodger, P. M.; Corni, S.; Walsh, T. R. GolP-CHARMM: First-Principles Based Force Fields for the Interaction of Proteins with Au(111) and Au(100). *J. Chem. Theory Comput.* **2013**, *9*, 1616–1630.

29. Ruan, L. Y.; Ramezani-Dakhel, H.; Chiu, C. Y.; Zhu, E. B.; Li, Y. J.; Heinz, H.; Huang, Y. Tailoring Molecular Specificity Toward a Crystal Facet: A Lesson From Biorecognition Toward Pt{111}. *Nano Lett.* **2013**, *13*, 840–846.

30. Emami, F. S.; Puddu, V.; Berry, R. J.; Varshney, V.; Patwardhan, S. V.; Perry, C. C.; Heinz, H. Prediction of Specific Biomolecule Adsorption on Silica Surfaces as a Function of pH and Particle Size. *Chem. Mater.* **2014**, *26*, 5725–5734.

31. Ramezani-Dakhel, H.; Mirau, P. A.; Naik, R. R.; Knecht, M. R.; Heinz, H. Stability, Surface Features, and Atom Leaching of Palladium Nanoparticles: Toward Prediction of Catalytic Functionality. *Phys. Chem. Chem. Phys.* **2013**, *15*, 5488–5492.

32. Pandey, R. B.; Heinz, H.; Feng, J.; Farmer, B. L.; Slocik, J. M.; Drummy, L. F.; Naik, R. R. Adsorption of Peptides (A3, Flg, Pd2, Pd4) on Gold and Palladium Surfaces by a Coarse-Grained Monte Carlo Simulation. *Phys. Chem. Chem. Phys.* **2009**, *11*, 1989–2001.

33. Coppage, R.; Slocik, J. M.; Briggs, B. D.; Frenkel, A. I.; Naik, R. R.; Knecht, M. R. Determining Peptide Sequence Effects That Control the Size, Structure, and Function of Nanoparticles. *ACS Nano* **2012**, *6*, 1625–1636.

34. Teranishi, T.; Miyake, M. Size Control of Palladium Nanoparticles and Their Crystal Structures. *Chem. Mater.* **1998**, *10*, 594–600.

35. Yancey, D. F.; Chill, S. T.; Zhang, L.; Frenkel, A. I.; Henkelman, G.; Crooks, R. M. A Theoretical and Experimental Examination of Systematic Ligand-Induced Disorder in Au Dendrimer-Encapsulated Nanoparticles. *Chem. Sci.* **2013**, *4*, 2912–2921.

36. Bedford, N.; Dablemont, C.; Viau, G.; Chupas, P.; Petkov, V. 3-D Structure of Nanosized Catalysts by High-Energy X-ray Diffraction and Reverse Monte Carlo Simulations: Study of Ru. *J. Phys. Chem. C* **2007**, *111*, 18214–18219.

37. Chakroune, N.; Viau, G.; Ammar, S.; Poul, L.; Veautier, D.; Chehimi, M. M.; Mangeney, C.; Villain, F.; Fievet, F. Acetate- and Thiol-Capped Monodisperse Ruthenium Nanoparticles: XPS, XAS, and HRTEM Studies. *Langmuir* **2005**, *21*, 6788–6796.

38. MacDonald, M. A.; Zhang, P.; Qian, H. F.; Jin, R. C. Site-Specific and Size-Dependent Bonding of Compositionally Precise Gold-Thiolate Nanoparticles from X-ray Spectroscopy. *J. Phys. Chem. Lett.* **2010**, *1*, 1821–1825.

39. Jadzinsky, P. D.; Calero, G.; Ackerson, C. J.; Bushnell, D. A.; Kornberg, R. D. Structure of a Thiol Monolayer-Protected Gold Nanoparticle at 1.1 Angstrom Resolution. *Science* **2007**, *318*, 430–433.

40. Keen, D. A.; Mcgreevy, R. L. Structural Modeling of Glasses Using Reverse Monte-Carlo Simulation. *Nature* **1990**, *344*, 423–425.

41. Heinz, H. Computational Screening of Biomolecular Adsorption and Self-Assembly on Nanoscale Surfaces. *J. Comput. Chem.* **2010**, *31*, 1564–1568.

42. Feng, J.; Slocik, J. M.; Sarikaya, M.; Naik, R. R.; Farmer, B. L.; Heinz, H. Influence of the Shape of Nanostructured Metal Surfaces on Adsorption of Single Peptide Molecules in Aqueous Solution. *Small* **2012**, *8*, 1049–1059.

43. Heinz, H.; Lin, T.-J.; Mishra, R. K.; Emami, F. S. Thermodynamically Consistent Force Fields for the Assembly of Inorganic, Organic, and Biological Nanostructures: The INTERFACE Force Field. *Langmuir* **2013**, *29*, 1754–1765.

44. Heinz, H.; Vaia, R. A.; Farmer, B. L.; Naik, R. R. Accurate Simulation of Surfaces and Interfaces of Face-Centered Cubic Metals Using 12−6 and 9−6 Lennard-Jones Potentials. *J. Phys. Chem. C* **2008**, *112*, 17281−17290.

45. Cremer, P. S.; Somorjai, G. A. Surface Science and Catalysis of Ethylene Hydrogenation. *J. Chem. Soc., Faraday Trans.* **1995**, *91*, 3671–3677.

46. Horiuti, I.; Polanyi, M. Exchange Reactions of Hydrogen on Metallic Catalysts. *Trans. Faraday Soc.* **1934**, *30*, 1164–1172.

47. Mattson, B.; Foster, W.; Greimann, J.; Hoette, T.; Le, N.; Mirich, A.; Wankum, S.; Cabri, A.; Reichenbacher, C.; Schwanke, E. Heterogeneous. Catalysis: The Horiuti-Polanyi Mechanism and Alkene Hydrogenation. *J. Chem. Educ.* **2013**, *90*, 613–619.

48. Newville, M. IFEFFIT: Interactive XAFS Analysis and FEFF Fitting. *J. Synchrotron Radiat.* **2001**, *8*, 322–324.

49. Moore, W. J.; Pauling, L. The Crystal Structures of the Tetragonal Monoxides of Lead, Tin, Palladium, and Platinum. *J. Am. Chem. Soc.* **1941**, *63*, 1392–1394.

50. Gaskell, T. F. The Structure of Braggite and Palladium Sulphide. *Z. Kristallogr.* **1937**, *96*, 203–213.

51. Wyckoff, R. W. G. *Cystal Structures*, 2nd ed.; Wiley Interscience: New York, 1963; Vol. 1, pp 7−83.

52. Petkov, V. RAD, a Program for Analysis of X-Ray-Diffraction Data from Amorphous Materials for Personal Computers. *J. Appl. Crystallogr.* **1989**, *22*, 387–389.

53. Petkov, V. Nanostructure by High-Energy X-ray Diffraction. *Mater. Today* **2008**, *11*, 28–38.

54. Billinge, S. J. L.; Kanatzidis, M. G. beyond Crystallography: The Study of Disorder, Nanocrystallinity and Crystallographically Challenged Materials with Pair Distribution Functions. *Chem. Commun.* **2004**, 749–760.

55. Petkov, V.; Ren, Y.; Kabekkodu, S.; Murphy, D. Atomic Pair Distribution Functions Analysis of Disordered Low-Z Materials. *Phys. Chem. Chem. Phys.* **2013**, *15*, 8544–8554.

56. Benmore, C. J.; Izdebski, T.; Yarger, J. L. Total X-ray Scattering of Spider Dragline Silk. *Phys. Rev. Lett.* **2012**, *108*, 178102–178105.

57. Gereben, O.; Jovari, P.; Temleitner, L.; Pusztai, L. A New Version of the RMC++ Reverse Monte Carlo Programme, Aimed at Investigating the Structure of Covalent Glasses. *J. Optoelectron. Adv. Mater.* **2007**, *9*, 3021–3027.

58. Bedford, N. M.; Bhandari, R.; Slocik, J. M.; Seifert, S.; Naik, R. R.; Knecht, M. R. Peptide-Modified Dendrimers as Templates for the Production of Highly Reactive Catalytic Nanomaterials. *Chem. Mater.* **2014**, *26*, 4082–4091.